Space Weather

RESEARCH ARTICLE
10.1029/2020SW002559

Special Section:
Heliophysics and Space Weather Studies from the Sun-Earth Lagrange Points

Evaluating the Performance of a Plasma Analyzer for a Space Weather Monitor Mission Concept

G. Nicolaou [1,2], R. T. Wicks[1], I. J. Rae[1], and D. O. Kataria[1]

[1]Mullard Space Science Laboratory, University College London, London, UK, [2]Southwest Research Institute, San Antonio, TX, USA

Key Points:
- The performance of a top hat electrostatic analyzer design is investigated in order to evaluate its accuracy in monitoring space weather
- The accuracy of the derived moments depends mainly on the plasma speed and temperature
- A fitting analysis method improves the accuracy of the derived parameters, and it is evaluated in typical coronal mass ejections and fast solar wind streams

Correspondence to:
G. Nicolaou,
georgios.nicolaou@swri.org

Citation:
Nicolaou, G., Wicks, R. T., Rae, I. J., & Kataria, D. O. (2020). Evaluating the performance of a plasma analyzer for a space weather monitor mission concept. *Space Weather*, *18*, e2020SW002559. https://doi.org/10.1029/2020SW002559

Received 9 JUN 2020
Accepted 3 NOV 2020
Accepted article online 13 NOV 2020

Abstract

We use historical analysis of solar wind plasma and coronal mass ejections to define the range of performance required for an ion analyzer for future space weather monitoring missions. We adopt the design of a top hat electrostatic analyzer, capable of measuring the plasma protons and constructing their three-dimensional distribution functions. The design is based on previous heritage instruments and allows monitoring of extreme space weather events. In order to evaluate the future observations and their analysis methods, we model the expected response of the instrument in simulated plasma conditions. We evaluate a novel analysis method which can determine on board the plasma bulk properties, such as density, velocity, and temperature from the statistical moments of the observed velocity distribution functions of the plasma particles. We quantify the accuracy of the derived parameters critical for space weather purposes, by comparing them with the corresponding input solar wind parameters. In order to validate the instrument design, we examine the accuracy over the entire range of the input parameters we expect to observe in solar wind, from benign to extreme space weather conditions. We also use realistic parameters of fast solar wind streams and interplanetary coronal mass ejections as measured by the Advanced Composition Explorer spacecraft, to investigate the performance of the example instrument and the accuracy of the analysis. We discuss the achieved accuracy and its relevance to space weather monitoring concepts. We address sources of significant errors, and we demonstrate potential improvements by using a fitting analysis method to derive the results.

Plain Language Summary

Space weather monitors should have the ability to constantly observe and characterize the solar wind plasma around Earth. We provide an initial plasma instrument design which monitors solar wind plasma within a wide range of parameters. We model the performance of the instrument and determine whether a novel analysis can accurately describe crucial space weather events. We simulate realistic plasma observations, which we analyze in a similar manner as we would do in a space weather mission concept. We characterize the quality of the observations by comparing the analysis results with the solar wind input we use to simulate the observations in the first place. Moreover, we evaluate the accuracy of the analysis results considering realistic space weather events and explain its relevance with space weather mission concepts. We explain the accuracy dependence on different factors, and we discuss how erroneous measurements can be improved with more computationally demanding onboard calculations or further on-ground analysis.

1. Introduction

Space weather represents a significant threat to national critical infrastructure and is recognized by both government and private industry at the national and international levels (e.g., Hapgood, 2012; Schrijver et al., 2015). Affected sectors include power, aviation, and satellites. A recent estimate of economic impact has calculated that a Carrington-level space weather event could cause a risk to around $1.1 trillion of the global integrated gross domestic product (GDP), approximately one quarter of the 5 year baseline global GDP projection (Oughton et al., 2016).

Space weather is fundamentally driven by solar activity and governed by the solar-terrestrial interaction. Magnetic reconnection in the dayside magnetopause enables solar wind plasma and energy to enter the magnetosphere. This energy is stored in the magnetotail, where it may be explosively released in the form of a substorm (e.g., Akasofu, 1964). Strong and prolonged driving of the magnetospheric system by the solar wind may lead to a geomagnetic storm, where the radiation belts become enhanced and energized

(e.g., Baker et al., 2013). Such strong and prolonged driving is typically caused by solar wind structuring, such us coronal mass ejections (CMEs) and stream interaction regions (SIRs) (e.g., Schwenn, 2006).

Since the magnetosphere is driven into storm time conditions by the solar wind, an effective space weather monitoring system requires knowledge of the interplanetary magnetic field and the solar wind plasma. Interplanetary phenomena of interest include, but are not limited to, high-speed solar wind streams, SIRs, solar energetic particle events, and interplanetary coronal mass ejections (ICMEs). In order to provide effective forecasts and warnings, space weather missions are expected to carry magnetometers and an in situ plasma instrument suite to measure the energetic particle environment and the bulk solar wind conditions during general and more extreme space weather.

Bulk ion plasma measurements play a vital role in refining ICME arrival time and magnitude estimates. Moreover, bulk plasma measurements are essential for identifying other solar wind transients, such as SIRs and high solar wind speed streams. Measurements of solar wind speed and densities are inputs into electron fluence models in the magnetosphere and to geomagnetic forecasts such as the planetary K index, K_p. Therefore, a successful space weather monitor requires reliable and accurate measurements of solar wind plasma bulk parameters, across and beyond their entire range of observed values.

Statistical studies over the past years examined the range of the solar wind bulk parameters within different structures and during different activity levels. These studies are crucial for the successful design of future missions, since they are informative for the definition of the measurement requirements. For instance, all hourly averaged solar wind speed measurements near 1 au between 1963 and 1999 were within the range from 100 to 1,000 km s^{-1} (McGregor et al., 2011; Watari et al., 2001). There is no reported solar wind speed or ICME speed measured at 1 au exceeding 2,500 km s^{-1}. Fast events include 2,150 (Baker et al., 2013; Liu et al., 2014; Russell et al., 2013), 1,700, and >1,850 km s^{-1} (Skoug et al., 2004). Solar wind densities range between 0.2 and 150 cm^{-3} during space weather events, and hence reliable and accurate measurements of bulk solar wind densities are required across this large range of values. Reliable and accurate solar wind temperatures are also required for the ambient solar wind and the plasma that is contained within ICMEs, covering the temperature range between a few eVs and <1,000 eV.

A successful space weather monitor should capture and characterize the crucial parameters of all the threatening space weather events. Practically, the range of the parameters characterizing the extreme events is not strictly determined. Although space weather monitors do not prioritize the accurate determination of all the plasma parameters for scientific analyses, they should be able to monitor both the background solar wind plasma in nominal condition and extreme events with their parameters exceeding drastically the nominal range. Moreover, a threatening event observed in space should be analyzed prior to its impact on Earth. Novel onboard analyses of the observations should be able to provide fast estimations of the plasma parameters and limit the required telemetry by reducing the amount of down-linked data. On the other hand, such methods may have several limitations, and alternative advanced onboard or on-ground methods should be considered. Therefore, the monitoring and especially the processing requirements for a space weather monitor are higher than those of a typical science plasma instrument.

Usually, space missions use Faraday cups or electrostatic analyzers to measure solar wind particles and determine their bulk parameters. Although Faraday cups are relatively simple, reliable, and steady, electrostatic analyzers are designed to construct the full velocity distribution function (VDF) of the plasma particles with remarkably high energy and angular resolution. In this study, we consider a specific electrostatic analyzer design which is able to sample the plasma particles over a wide range of energies and flow directions.The instrument should also have the appropriate energy and angular resolution in order to resolve typical fast solar wind streams and ICMEs over the background solar wind plasma. Importantly, for a space weather application, an electrostatic analyzer should be able to perform decently well even during large solar energetic proton events. We model the expected observations taking into account realistic technological limitations and statistical uncertainties, and we quantify the accuracy of a simple analysis method as a function of the bulk parameters. Such a study drives the design of future instruments and helps in understanding their performance. In section 2 we present the instrument design and the methods we use to model its observations and to derive the plasma bulk parameters. In section 3 we present the accuracy test results within a broad range of the simulated plasma parameters. In section 4, we evaluate the accuracy of our instrument considering the parameters of a fast ICME recorded by Advance Composition Explorer, while in section 5, we evaluate it for a fast solar wind stream. In section 6, we discuss in detail our results.

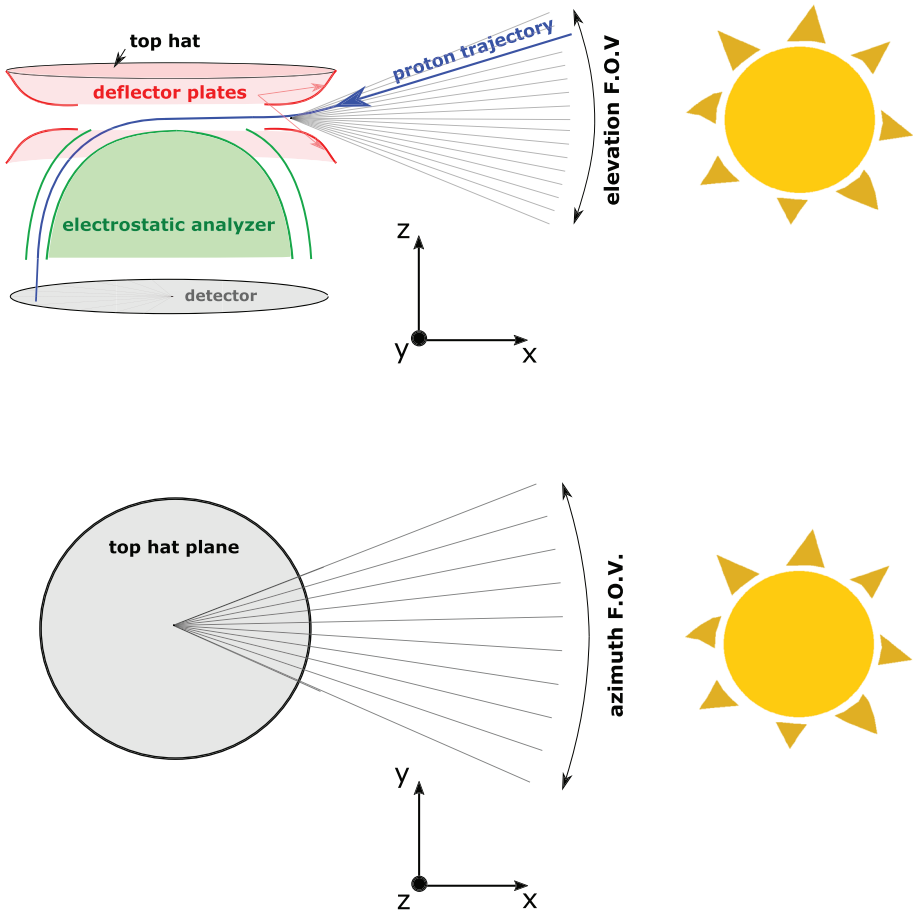

Figure 1. Schematic of our instrument design and its measurement principle showing the (top) elevation and (bottom) azimuth field of view. The aperture deflectors (red color) scan through the elevation angle which is the angle between the particle velocity vector and the top hat plane (*x*-*y* plane). The electrostatic analyzer (green) bends particles with specific energy per charge and guides them toward the detector (gray). The azimuth angle is the angle between the *x* axis and particle velocity vector projection on the top hat plane, and it is resolved on the detector azimuth sectors, as specific azimuth sectors record particles coming from specific azimuth directions within their resolution.

Among others, we identify several sources of errors in the derived moments, and we examine an alternative analysis method to derive the plasma bulk parameters with improved accuracy. Finally, in section 7 we summarize our conclusions.

2. Methods

2.1. Instrument Design and Operation

We examine solar wind proton measurements, obtained by a typical top hat electrostatic sensor design. Our concept instrument is based on Solar Wind Analyser's Electron Analyser System (SWA-EAS, Owen et al., 2020) on board Solar Orbiter, while similar electrostatic analyzer designs have provided successful measurements of plasma species in several space plasma environments (e.g., Barabash et al., 2006; Johnstone et al., 1997; McComas et al., 2017; Nilsson et al., 2007). In Figure 1, we show a schematic of our instrument and a single proton trajectory through its structure, in order to demonstrate the measurement principle. The design comprises an aperture deflector unit, electrostatic analyzer, and a detector that can be either a Multi-Channel Plate (MCP) or a series of Channel Electron Multipliers (CEMs). The electrostatic potential applied between the aperture deflector plates bends protons guiding specific trajectories through the instrument aperture. Scanning through a range of potentials across the deflector plates, the instrument samples the particle flux as a function of the elevation angle, defined as the angle between the velocity vector and the top hat plane (*x*-*y* plane). The instrument scans the elevation directions in 16 discrete steps between −22.5° and +22.5° with respect to the spacecraft-Sun line (*x* axis). In this study, we consider an

instrument that resolves each elevation direction with resolution $\Delta\Theta \sim 2.8°$, typically determined at the full width half maximum of the instrument's response curve, for fixed look directions. The elevation angle resolution is limited by the geometric properties of the instrument, such as the size of the aperture and the electrostatic analyzer. We note, however, that the resolution could be a function of the particle direction and has to be determined from a detailed calibration. Particles which enter the aperture are heading toward the electrostatic analyzer (ESA), a structure of two shells of partial concentric spheres (ESA domes). We achieve measurements of protons in different energies per charge E/q, by tuning the voltage between the ESA's domes, in 64 discrete steps. With the proper high-voltage power supply (HVPS), the instrument measures solar wind protons between 50 eV/q and 36 keV/q, which, for the proton mass m_p 1.67×10^{-27} kg and elementary charge $q = 1$ corresponds to a speed $U = \sqrt{\frac{2E}{m_p}}$ range between ~100 and ~2,600 km s^{-1}. The energy acceptance for each energy step is $\frac{\Delta E}{E} = 2\frac{\Delta U}{U} = 10\%$. As is typical of the top hat analyzer geometry, the azimuth angles are sampled simultaneously. In the design here, the azimuth direction is resolved by nine azimuth sectors mounted on the electronic detector plane, covering the range between −22.5° and +22.5° with respect to the average aberrated direction of the solar wind. The resolution in azimuth direction is $\Delta\Phi = 5°$, which according to previous designs is optimal for limited electronic cross-talk between the azimuth sectors. In order to obtain measurements of the three-dimensional (3-D) distribution function, the instrument scans through the entire energy range, for each elevation angle, with the azimuth direction being resolved simultaneously by the azimuth sectors. The acquisition time for each energy elevation step is $\Delta\tau \sim 1$ ms; therefore, the instrument completes a full 3-D scan cycle in $64 \times 16 \times \Delta\tau \sim 1$ s.

2.2. Expected Counts

We use the well-established forward modeling method (e.g., Cara et al., 2017; Elliott et al., 2016; Kim et al., 2020; Kessel et al., 1989; Martz et al., 1993; Nicolaou, McComas, Bagenal, Elliott, & Wilson, 2015; Nicolaou et al., 2014, 2018, 2019; Nicolaou & Livadiotis, 2020; Nicolaou, Livadiotis, & Wicks, et al., 2020; Nicolaou, Wicks, et al., 2020; Wilson et al., 2008, 2017) in order to simulate solar wind proton observations by our instrument design. We assume that the plasma protons reside in classical thermal equilibrium with their velocities $\vec{u}$ following the isotropic (single temperature) Maxwell distribution function:

$$f(\vec{u}) = N\left(\frac{m}{2\pi k_B T}\right)^{\frac{3}{2}} \exp\left(-\frac{m(\vec{u}-\vec{V})^2}{2k_B T}\right), \tag{1}$$

where N, $\vec{V}$, and T are the plasma number density, bulk velocity, and temperature, respectively, and k_B is the Boltzmann constant. For a specific distribution function $f(\vec{u})$, the number of particles that are detected in each U, Θ, and Φ pixel of the instrument is

$$C(U,\Theta,\Phi) = \int_{U-\frac{\Delta U}{2}}^{U+\frac{\Delta U}{2}} \int_{\Theta-\frac{\Delta\Theta}{2}}^{\Theta+\frac{\Delta\Theta}{2}} \int_{\Phi-\frac{\Delta\Phi}{2}}^{\Phi+\frac{\Delta\Phi}{2}} \int_{t-\frac{\Delta\tau}{2}}^{t+\frac{\Delta\tau}{2}} A_{\text{eff}}(u,\theta,\phi,t) f(u,\theta,\phi,t) u^3 \, du \cos\theta d\theta \, d\phi \, dt, \tag{2}$$

where A_{eff} is the effective aperture of the instrument. For simplicity, we assume that A_{eff} is only a function of the elevation angle Θ, that is, $A_{\text{eff}}(\Theta) = A_0 \cos(\Theta)^{-1}$. We approximate this integral numerically using the midpoint rule so that

$$C(U,\Theta,\Phi) \sim G(U,\Theta,\Phi) f(U,\Theta,\Phi) U^4 \Delta\tau, \tag{3}$$

where $G = A_0 \frac{\Delta U}{U} \Delta\Theta\Delta\Phi$ is the geometric factor of the instrument, determined by its geometry and detection efficiency. The geometric factor is in general different for each U, Θ, Φ, and sometimes it is also a function of time. However, here we simplify by considering a constant value $G = 7.8 \times 10^{-6}$ cm^2 sr.

2.3. Dead Time of the Detector

Ideally, the instrument would record all the expected counts given by Equation 3. However, counting systems do not have the ability to record events at infinite rate. Detectors do not distinguish between two separate events, unless the time separating the two events is larger than the dead time t_d, which characterizes the response of the detector and the electronics. Therefore, from the C expected in one sample period $\Delta\tau$, only C_s are registered (Knoll, 2000). Assuming that t_d is constant (nonparalyzable model), then for each sample

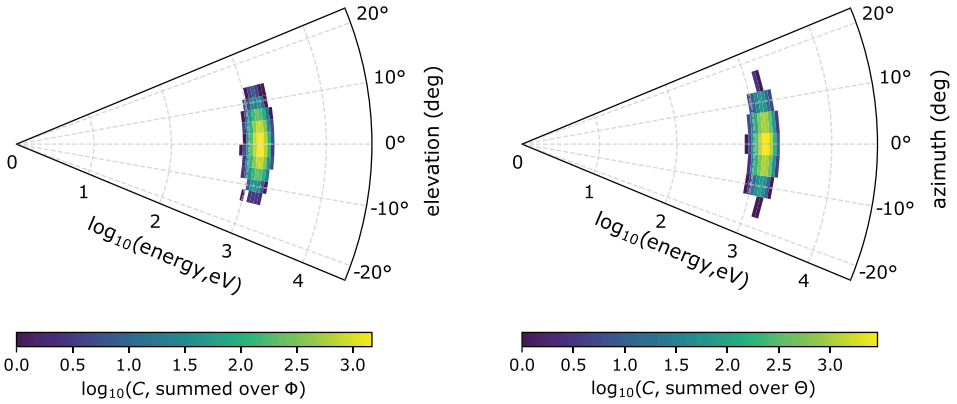

Figure 2. Modeled observations for plasma with $N = 10\,\mathrm{cm}^{-3}$, $\vec{V} = 500\,\mathrm{km\,s}^{-1}$ toward $\hat{x}$ ($\Theta = \Phi = 0°$), and $T = 10\,\mathrm{eV}$. The left panel shows the observed counts as a function of elevation (summed over the azimuth directions), and the right panel shows the observed counts as a function of azimuth direction (summed over the elevation directions).

within $\Delta\tau$, the detector does not register events for a time interval $C_s t_d$. The expression for the lost events in each sample is

$$C - C_s = C_s C \frac{t_d}{\Delta\tau}, \tag{4}$$

and solving for the registered counts

$$C_s = \frac{C}{1 + \frac{t_d}{\Delta\tau} C}. \tag{5}$$

The detector electronics we consider for our instrument design are characterized by $t_d = 10^{-7}$ s. The registered counts C_s have an asymptotic behavior, approaching $C_s \to \Delta\tau/t_d$ as $C \to \infty$ (see also Figure 3). A specific detector saturates as the plasma flux increases and more particles arrive on the detector's surface within t_d and cannot be registered as separate events.

2.4. Counting Statistics

The detector measures the number of particles within a certain level of uncertainty. Typically, counted events follow the Poisson distribution function; therefore, we assume detector measurements C_m with probability

$$P(C_m) = e^{-C_s} \frac{C_s^{C_m}}{C_m!}. \tag{6}$$

We model observations $C_m(U, \Theta, \Phi)$ for specific sets of N, $\vec{V}$, and T, in order to evaluate the instrument design for expected solar wind conditions. In Figure 2 we show the modeled observations in the instrument's frame, considering plasma with $N = 10\,\mathrm{cm}^{-3}$, $\vec{V} = 500\,\mathrm{km\,s}^{-1}$ in the $\hat{x}$ direction, and $T = 10\,\mathrm{eV}$. The left panel of Figure 2 shows the counts summed over azimuth direction $\sum_{\Phi} C_m$, as a function of Θ, while the right panel shows the counts summed over elevation direction $\sum_{\Theta} C_m$, as a function of Φ.

2.5. Pseudomeasurement Analysis

For scientific and quantitative applications, it is essential to convert the measurements to physical quantities, such as density, speed, and temperature. We calculate these plasma bulk parameters by analyzing the observations. The first step of this analysis is to correct for the dead time of the detector using the inverse of Equation 5:

$$C_{out} = \frac{C_m}{1 - \frac{t_d}{\Delta\tau} C_m}, \tag{7}$$

where the recovered counts C_{out} is the best estimation of the expected counts in actual applications. Nevertheless, due to Poisson measurement uncertainties, C_m can be larger than $\Delta\tau/t_d$, leading to negative C_{out},

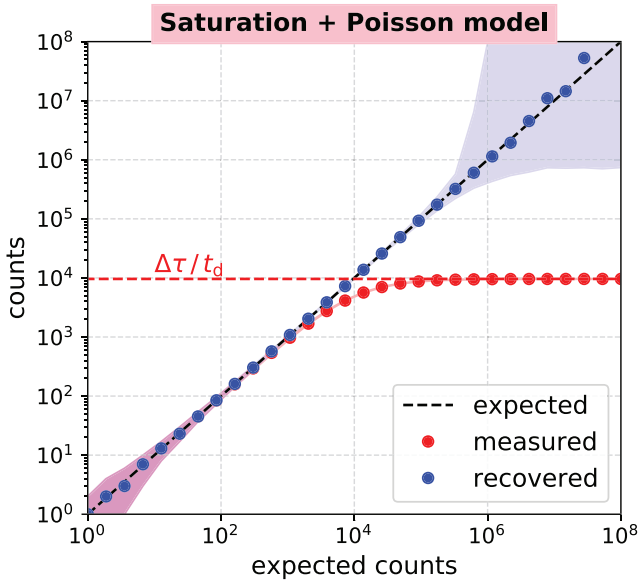

Figure 3. The measured counts C_{m} estimated by Equations 5 and 6 (red) and the recovered C_{out} (blue) counts estimated by Equation 7 as a function of the expected counts C. The dots correspond to the median values over 1,000 simulated samples, while the shadowed area is bounded by the 10% and the 90% quartiles. The black dashed line is the identity function, while the red dashed indicates the $\Delta\tau/t_{\mathrm{d}}$ ratio.

which is of course invalid. Therefore, the formula in Equation 7 needs to be restricted. For the purposes of this study, negative C_{out} values are set to the maximum value recorded within the sample. Then, using the inverse of Equation 3, we get the velocity distribution function resolved in U, Θ, and Φ bins:

$$f_{\mathrm{out}}(U,\Theta,\Phi)=\frac{C_{\mathrm{out}}(U,\Theta,\Phi)}{GU^4\Delta\tau}. \tag{8}$$

We calculate the bulk properties of the observed plasma by deriving the statistical velocity moments of f_{out}. The plasma density is

$$N_{\mathrm{out}}=\sum_U\sum_\Theta\sum_\Phi f_{\mathrm{out}}(U,\Theta,\Phi)U^2\Delta U'\cos\Theta\Delta\Theta'\Delta\Phi', \tag{9}$$

the bulk velocity components are

$$V_{i,\mathrm{out}}=\frac{1}{N_{\mathrm{out}}}\sum_U\sum_\Theta\sum_\Phi U_i f_{\mathrm{out}}(U,\Theta,\Phi)U^2\Delta U'\cos\Theta\Delta\Theta'\Delta\Phi' \tag{10}$$

from which we get the bulk speed

$$V_{\mathrm{out}}=\sqrt{\sum_{i=1}^{3}V_{i,\mathrm{out}}^2}. \tag{11}$$

The temperature tensor elements $T_{\mathrm{out}}^{i,j}$ are

$$T_{\mathrm{out}}^{i,j}=\frac{1}{N_{\mathrm{out}}}\sum_U\sum_\Theta\sum_\Phi m(w^{i,j})^2 f_{\mathrm{out}}(U,\Theta,\Phi)U^2\Delta U'\cos\Theta\Delta\Theta'\Delta\Phi', \tag{12}$$

with $w^{i,j}=U_i-V_{j,\mathrm{out}}$. Finally, the scalar temperature T_{out} is

$$T_{\mathrm{out}}=\frac{1}{3}\left(\sum_{i=1}^{3}T_{\mathrm{out}}^{i,i}\right). \tag{13}$$

In Equations 9–12, the summation steps $\Delta U'$, $\Delta\Theta'$, and $\Delta\Phi'$ are the step sizes between consecutive U, Θ, and Φ sampling pixels, respectively.

The comparison between the derived N_{out}, V_{out}, and T_{out} and the corresponding input N, V, and T quantifies the accuracy of the derived parameters. In the next section, we show the detailed accuracy quantification for our model instrument.

3. Simulation Results

For each combination of the input solar wind bulk parameters N, V, and T, we model 10 measurement samples, which we analyze to calculate the ratios $\langle N_{\mathrm{out}}\rangle/N$, $\langle V_{\mathrm{out}}\rangle/V$, and $\langle T_{\mathrm{out}}\rangle/T$. These ratios indicate the average relative error of the derived parameters. The purpose of calculating the average errors over 10 samples is to account for the Poisson statistical error governing the measurements. The top row panels in Figure 4 show $\langle N_{\mathrm{out}}\rangle/N$, while the middle row panels show $\langle V_{\mathrm{out}}\rangle/V$, and the bottom row panels show $\langle T_{\mathrm{out}}\rangle/T$, as functions of the input N and T, for input speed (left) $V=400$, (middle) $V=800\,\mathrm{km\,s^{-1}}$, and (right) $V=1{,}500\,\mathrm{km\,s^{-1}}$. The isocontours on each plot show the logarithm of the number of U, Θ, and Φ instrument pixels which record a measurement ($C_{\mathrm{out}}>1$). For instance, the region below Isocontour 1 corresponds to combinations of plasma parameters for which the velocity distribution function is resolved in a fewer than 10 pixels of our plasma sensor.

Although the error of the derived parameters has a limited dependence on the plasma density, there are misestimations of N_{out} and T_{out}, prominent in the range $N>100\,\mathrm{cm^{-3}}$, for $V=800$ and $1{,}500\,\mathrm{km\,s^{-1}}$. Such strong misestimations are due to strong dead time saturations which prevent the accurate recovery of the actual counts. As the density and/or speed increases, the expected counts increase and the registered counts get closer to the asymptotic $\frac{\Delta\tau}{t_{\mathrm{d}}}$, which magnifies the error of the recovered counts C_{out} (see also Figure 3).

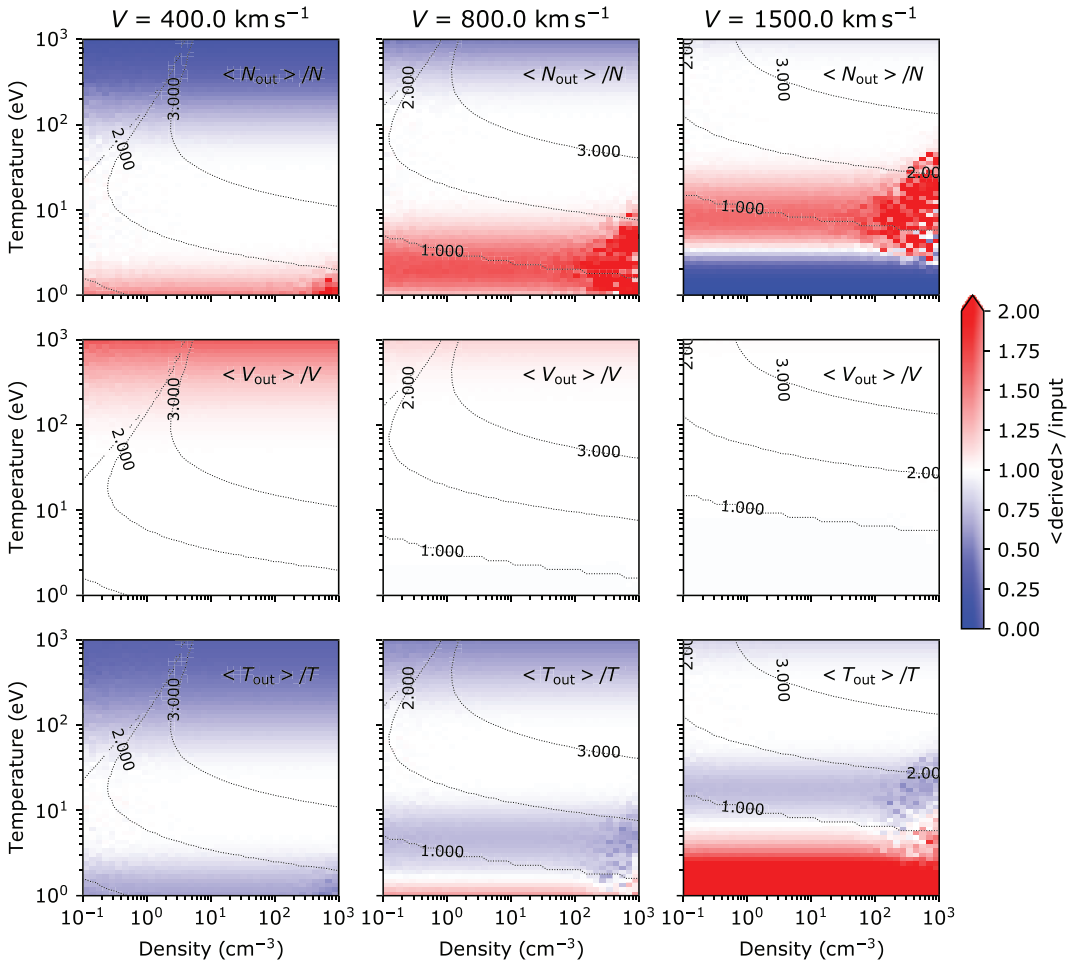

Figure 4. Ratios of the average derived plasma parameters over the corresponding input plasma parameters, presented as functions of the input plasma parameters. (top row) $\langle N_{out}\rangle/N$, (middle row) $\langle V_{out}\rangle/V$, and (bottom row) $\langle T_{out}\rangle/T$ as functions of N and T, shown for three different input plasma bulk speeds (left) $V = 400\,km\,s^{-1}$, (middle) $V = 800\,km\,s^{-1}$, and (right) $V = 1{,}500\,km\,s^{-1}$. The gray isocontours on each plot indicate the logarithm of the number of U, Θ, and Φ pixels with valid measurement ($C_{out} > 1$).

There are also significant misestimations associated with poor sampling of the velocity distribution functions. For instance, the plasma density and temperature are significantly misestimated for $V = 1{,}500\,km\,s^{-1}$ and $T < 10\,eV$. For these specific input parameters, the plasma distributions are practically sampled in fewer than 10 pixels of the instrument.

For a slow solar wind with $V = 400\,km\,s^{-1}$ (left column in Figure 4) the derived density is overestimated within the low-temperature range ($T < 2eV$), while it is underestimated within the high-temperature range ($T > 80\,eV$). For the same bulk speed, the derived speed is overestimated for $T > 100\,eV$, and the temperature is underestimated for $T < 20\,eV$ and $T > 100\,eV$. For solar wind with $V = 800\,km\,s^{-1}$ (middle column in Figure 4), the density is overestimated for $T < 10\,eV$ and underestimated for $T > 300\,eV$, while the derived bulk speed is slightly overestimated for $T > 300\,eV$. The derived temperature is misestimated for $T < 10\,eV$ and $T > 200\,eV$. Finally, for $V = 1{,}500\,km\,s^{-1}$ (right column in Figure 4), the density and temperature are significantly misestimated (either overestimated or underestimated) for $T < 30\,eV$, while the speed is accurately estimated over the entire N and T range we examine here.

It is very important for a space weather monitor to reduce data transmission and increase the efficiency of the observation processing. The exact details of distribution functions are not required for space weather forecasting. But N, $\vec{V}$, and, to a lesser degree, T, are required. We remind the reader that the derived parameters are calculated from the velocity moments of the observed distribution functions. This method

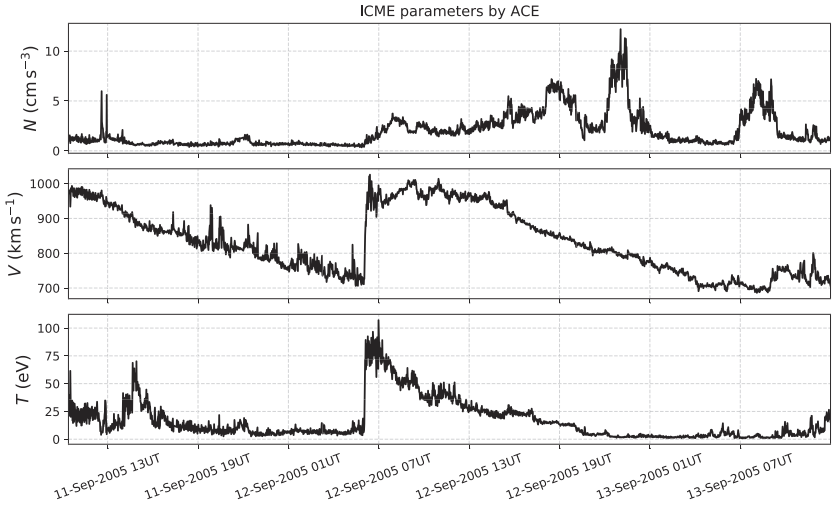

Figure 5. Time series of solar wind (top) density, (middle) speed, and (bottom) temperature for two ICMEs observed by ACE between 11 and 13 September 2005.

is computationally cheap and therefore optimal for continuous onboard calculations of the plasma parameters. Although it has its benefits, moments calculation on board has a number of limitations which we discuss in section 6, emphasizing that it is potentially useful to analyze the 3-D distribution function with different techniques such as fitting Maxwellian functions to the observations.

4. ICME Data Application

A successful space weather mission at the Lagrangian point L_1 must prioritize the monitoring and characterization of ICMEs which can impact Earth. In this section, we quantify the accuracy of the derived moments, considering realistic plasma conditions during a very fast ICME as observed by the Advanced Composition Explorer (ACE) spacecraft. ACE was launched in 1997 and orbits L_1 (Stone et al., 1998). The spacecraft carries a series of instruments, which monitor the interplanetary medium, providing real-time measurements that are crucial for forecasting space weather. The Solar Wind Electron, Proton, and Alpha Monitor (SWEPAM) on board ACE (McComas et al., 1998) measures the directional flux of the primary solar wind components. The ion sensor measures the plasma particles within the energy range from 0.26 to 36 keV, and its high resolution measurements can provide the proton bulk properties every 64 s. We use SWEPAM level 2 data found at https://cdaweb.gsfc.nasa.gov/cgi-bin/eval2.cgi, in order to evaluate the measurements of our instrument, considering examples of fast ICMEs measured at L_1 by ACE and registered

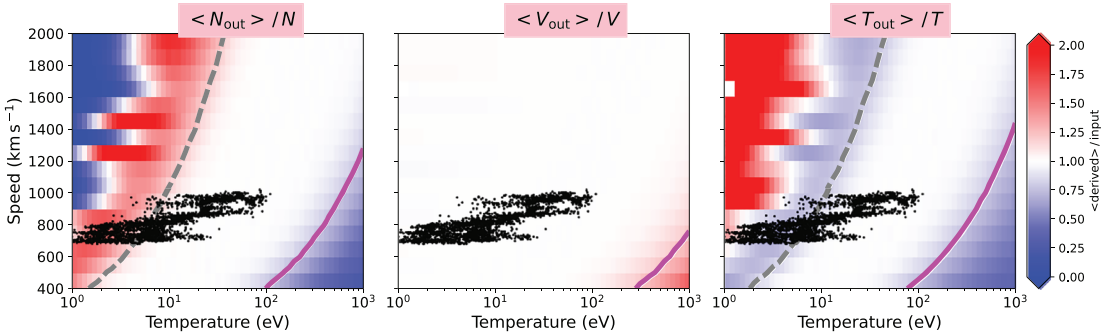

Figure 6. The speed as a function of temperature for the ICME observations in Figure 5 overplotted on the corresponding matrices of (left) $\langle N_{out}\rangle/N$, (middle) $\langle V_{out}\rangle/V$, and (right) $\langle T_{out}\rangle/T$. The solid magenta and dashed gray lines are selected isocontours of 20% error of the corresponding plasma parameters. Significant misestimations on the left-hand side of the dashed gray line are due to a poor sampling of beam-like (narrow) distributions which are sampled in only a few pixels. Significant misestimations on the right-hand side of the solid magenta line are associated with undersampled distributions which have particles with velocities beyond the sampled velocity range.

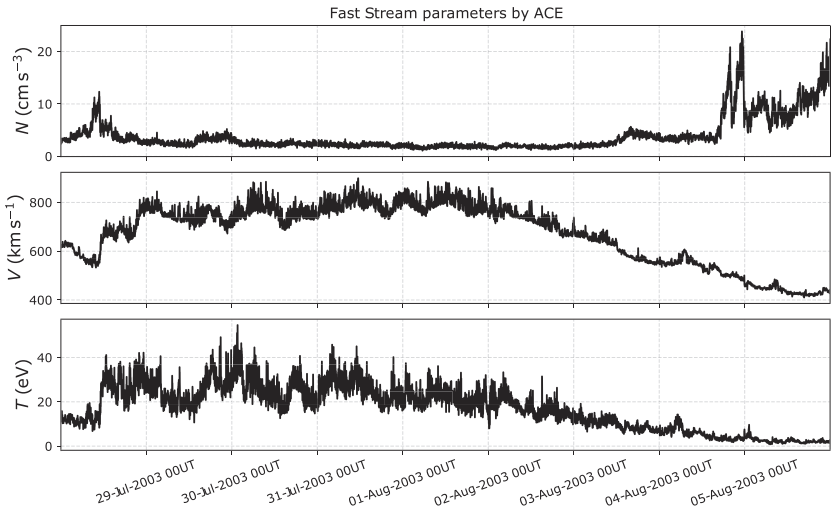

Figure 7. Time series of solar wind (top) density, (middle) speed, and (bottom) temperature for an interval between 28 July 2003 and 6 August 2003, during which ACE observed a fast solar wind stream.

by Richardson and Cane (2010). This evaluation is crucial for the determination of the instrument's accuracy in expected, extreme conditions. Although SWEPAM accuracy suffers occasionally from penetrating radiation (e.g., Skoug et al., 2004), we consider the available measurements as the best way to evaluate our instrument in realistic plasma conditions.

In Figure 5, we show the time series of two fast ICMEs recorded by ACE from 11 September 2005 at 10:00 to 13 September 2005 at 13:00. The instrument captures the decaying phase of the first ICME, before the sharp speed and temperature increase due to the second ICME in the morning of 12 September 2005. The maximum speed within the entire time interval is ~1,000 km s^{-1}. Our analysis in section 3 shows that the accuracy of the derived moments does not strongly depend on the plasma density over the examined range. Therefore, for the evaluation here, we examine the performance of our instrument and the accuracy of the derived moments as a function of V, and T, for a typical density value $N \sim 5\,\mathrm{cm}^{-3}$. In Figure 6, we show the accuracy of the simulated instrument as the ratio between $\langle N_{\mathrm{out}} \rangle / N$, $\langle V_{\mathrm{out}} \rangle / V$, and $\langle T_{\mathrm{out}} \rangle / T$. On each panel, we overplot the speed as a function of temperature for the ICME in Figure 5, showing that the majority of the data points correspond to areas with a relatively small error (white color area). We also draw selected isocontours of 20% error in the estimated parameters. Strong misestimations of the plasma parameters in regions on the left-hand side of the gray-dashed isocontours are associated with beam-like distributions which are sampled in just a few pixels of the instrument. Strong misestimations of the parameters in regions on the right-hand side of the solid-magenta isocontours are associated with broad distributions with particle velocities beyond the sampling range of our instrument.

As mentioned in section 3, the calculation of the velocity moments provides fast estimations of the plasma bulk parameters, but the instrument's limited detection efficiency, energy, and angular range and resolution reduce the accuracy of the specific method. In section 6, we extensively discuss these limitations and their impact on the measurements. Nevertheless, it is important to investigate alternative analysis methods to improve the accuracy when needed. In Appendix A, we investigate the accuracy of five fast ICMEs registered in Richardson and Cane (2010), using the reduced χ^2 fitting method.

5. Fast Solar Wind Streams Data Application

In this section, we investigate the accuracy of the plasma parameters derived from observations of fast solar wind streams over a slow background solar wind. Monitoring and characterizing such space weather events is vital for space weather missions, especially at Lagrangian point L_5, mainly because solar wind measurements at any point in the heliosphere are crucial for accurate modeling. Second, a space weather monitor at L_5 can monitor wide CMEs which will impact Earth and have connectivity to the shock front. In Figure 7, we show solar wind parameters as derived from ACE observations between 28 July and 6 August 2003. Within this time interval there is a fast solar wind stream with speed exceeding 800 km s^{-1} just after 29 July. On 2

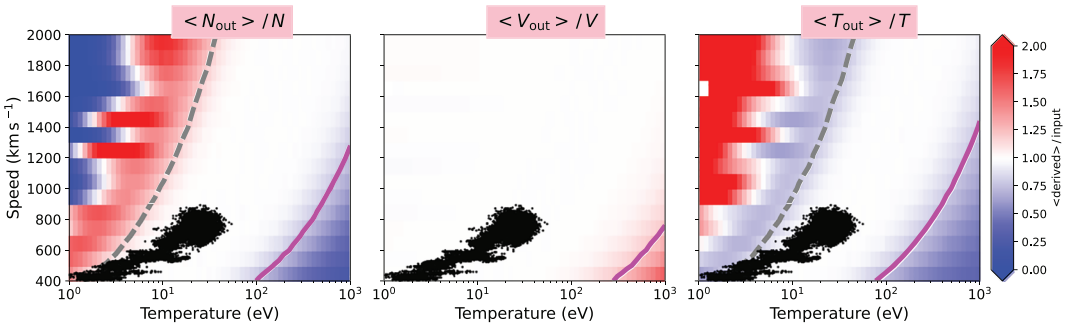

Figure 8. The speed as a function of temperature for the fast solar wind stream observations in Figure 7 overplotted on the corresponding matrices of (left) $\langle N_{out}\rangle/N$, (middle) $\langle V_{out}\rangle/V$, and (right) $\langle T_{out}\rangle/T$. The solid magenta and dashed gray lines are selected isocontours of 20% error of the corresponding plasma parameters. Significant misestimations on the left-hand side of the dashed gray line are due to poor sampling of beam-like distributions. Significant misestimations on the right-hand side of the solid magenta line are associated with undersampled distributions which have particles with velocities beyond the sampled velocity range.

August, the speed drops gradually and reaches ~400 km s^{-1} after 5 August. The observed high-speed stream has lower density and higher temperature than the slower solar wind within the time interval. In Figure 8, we show the accuracy plots $\langle N_{out}\rangle/N$, $\langle V_{out}\rangle/V$, and $\langle T_{out}\rangle/T$ for our model, and we overplot the speed as a function of temperature for the event in Figure 7. The majority of the data points correspond to areas with a relatively small error (white color area). As in Figure 6, we show selected isocontours of 20% error in the estimated parameters.

For the example we show here, the statistical moments analysis calculates with practically no error the solar wind speed, which is the most crucial parameter to identify and characterize the fast and slow streams and their interaction regions. Nevertheless, in Appendix B, we investigate potential accuracy improvements by using the reduced χ^2 fitting method to analyze observations of fast and slow solar wind streams. For our investigation, we use input parameters of four time intervals containing fast solar wind streams observed by ACE and registered by Xystouris et al. (2014).

6. Discussion

Our study models the expected simple onboard moment calculation results for observations of solar wind protons by an ESA design on a space weather mission concept. With a standard analysis of the modeled observations we derive the plasma parameters and calculate their relative error. Our error matrices in section 3 summarize the performance of the instrument as a function of the plasma parameters. The accuracy of the derived plasma parameters depends mainly on the plasma speed and temperature. The accuracy requirements for each of the plasma parameters are potentially different, depending on the mission concept. For instance, a space weather mission at Langrangian point L_1 prioritizes the monitoring of extreme events and the evaluation of their potential threat. In such a case, an in situ plasma instrument must prioritize the accurate determination of the plasma speed and density of such an event in order to estimate its arrival time at Earth and the particle flux associated with it. On the other hand, a space weather monitor at L_5 focuses on the accurate characterization of the background solar wind, as the angular width of extreme ICMEs do not often exceed ~60° which is the minimum width required for an ICME at L_5 to impact Earth. In this section we address sources of errors in the estimated parameters within the range of the observed plasma. We then demonstrate how an alternative method can overcome significant misestimations within a wide range of the plasma parameters. Such an alternative method should be considered for future operations if the mission concept prioritizes high accuracy in the specific range of the plasma parameters where the novel calculation of moments returns significant misestimations.

6.1. Sources of Errors

The velocity distribution function is constructed by the observations in the instrument frame (U, Θ, Φ). The accurate derivation of the plasma parameters depends on the energy and angular resolution of the instrument and the shape of the plasma VDF (for details see Nicolaou et al., 2019). The shape of the distribution is a function of the plasma bulk parameters (see Equation 1). For instance, as the plasma bulk speed

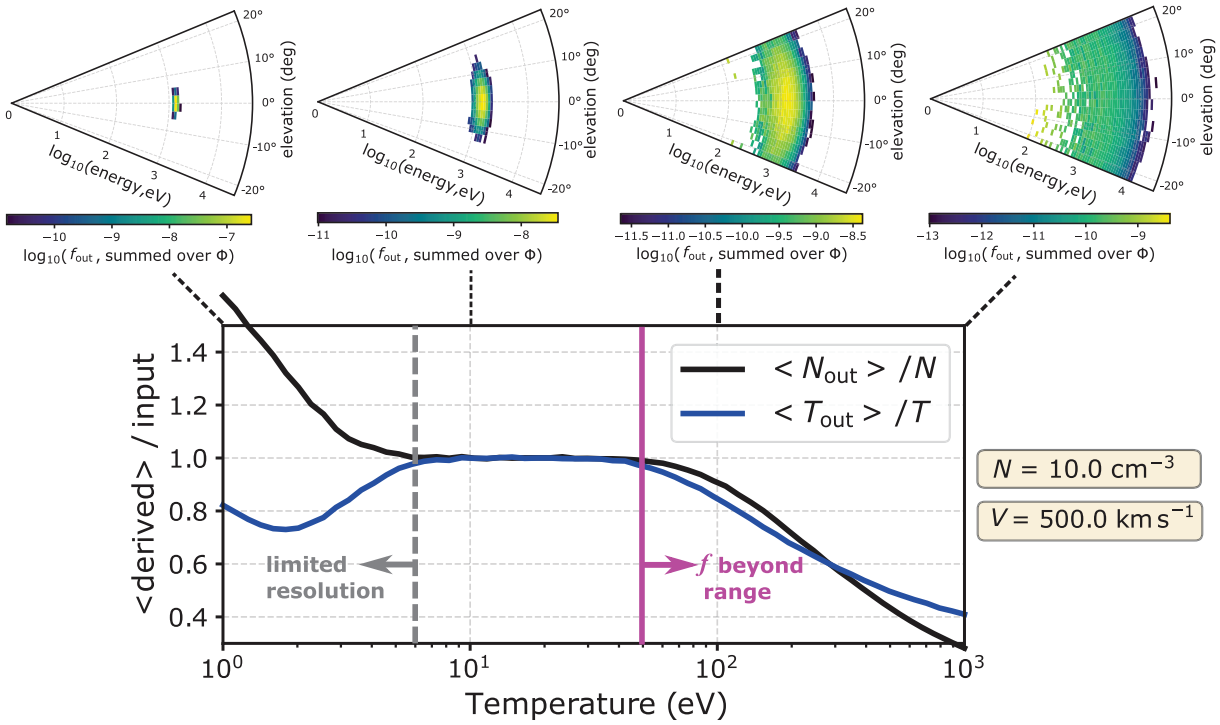

Figure 9. Normalized derived density $\langle N_{out}\rangle/N$ (black) and temperature $\langle T_{out}\rangle/T$ as functions of the input temperature T, for plasma with $N = 10\,\mathrm{cm}^{-3}$ and $V = 500\,\mathrm{km\,s}^{-1}$ toward $\hat{x}$ ($\Theta = \Phi = 0°$). On the top, we show distribution functions f_{out} summed over azimuth directions, as functions of energy and elevation direction, constructed from observation of plasma with (from left to right) $T = 1$ eV, $T = 10$ eV, $T = 100$ eV, and $T = 1{,}000$ eV.

increases, the distribution shifts to higher energy/speed (U) channels. The instrument's absolute resolution decreases with U, since $\Delta U/U$ is constant. As a result, faster distributions will be resolved in fewer energy pixels U. In addition, as a distribution with fixed width shifts to higher energies, its width spreads over fewer elevation and azimuth pixels resulting in reduced resolution. Moreover, as the temperature decreases, the thermal spread of the particles is reduced. Therefore, relatively fast and cold plasma is resolved in limited (U, Θ, Φ) pixels, reducing the accuracy of the numerical calculations in Equations 9–13. Consider, for example, the extreme case for which the distribution function resides within the range of only one U, Θ, Φ. In such a case, there is no information about the shape of the distribution function, since there is only one measurement for it. However, the velocity V is known with the resolution of the instrument, as the peak is clearly identified. Thus, V is often the most accurately measured moment. In Figure 9, we show the ratios $\langle N_{out}\rangle/N$ and $\langle T_{out}\rangle/T$ as a function of T. For the examples shown, we set $N = 10\,\mathrm{cm}^{-3}$, and $V = 500\,\mathrm{km\,s}^{-1}$. The misestimation of the derived parameters in the low-temperature range ($T < 10$ eV) is due the limited resolution of f.

Additionally, the energy and the field-of-view range of plasma instruments are finite. Each plasma instrument design is optimized to measure particles in specific environments, but sometimes, the energy and/or the angular direction of the plasma particle velocities are beyond the instrument's energy and field-of-view range, respectively. In such cases, the distribution is not fully resolved, and the plasma moments are misestimated. For instance, Figure 9 shows that as T increases, the angular spread of the particle velocities increases, and eventually, a portion of the particles sits outside the instrument's field of view, causing a systematic misestimation of N_{out} and T_{out}.

Lastly, in the case of any particle instrument, the detector's limited response time (in our case characterized by a dead time $t_d = 10^{-7}$ s) introduces systematic misestimations of the plasma parameters. The expected count rate is proportional to the particle flux through the instrument's aperture and increases with increasing density and/or speed. Although in our analysis we use Equation 7 to correct for the nonregistered counts, the accuracy of the specific formula is significantly reduced as the measured counts $\rightarrow \Delta\tau/t_d$. These limitations

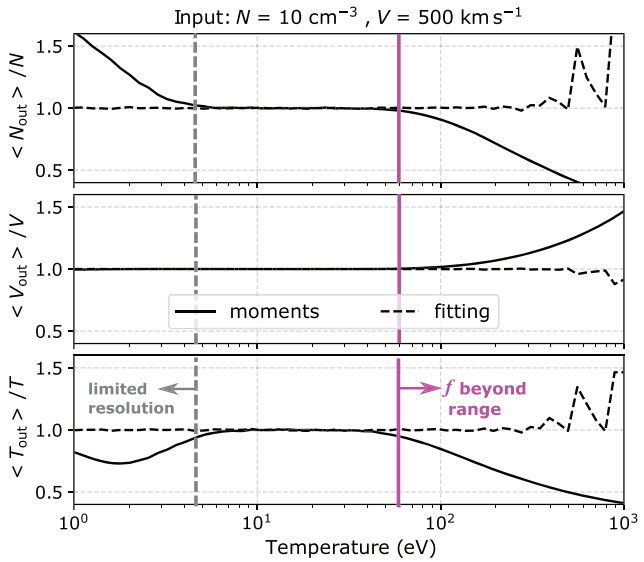

Figure 10. Normalized plasma bulk parameters (top) $\langle N_{\rm out}\rangle/N$, (middle) $\langle V_{\rm out}\rangle/V$, and (bottom) $\langle T_{\rm out}\rangle/T$, derived by the moments analysis (solid line) and by the fitting (dashed) analysis method, as functions of T, considering plasma with $N = 10\,{\rm cm}^{-3}$ and $V = 500\,{\rm km\,s}^{-1}$. The vertical dashed gray and solid magenta lines indicate the boundaries of the optimal temperature range for which both methods provide accurate plasma parameters. For temperatures on the left-hand side of the dashed gray line, the distributions are poorly resolved by the instrument. For temperatures on the right-hand side of the solid magenta line, the distributions have particles with velocities beyond the sampled velocity range. The errors of the derived moments in the low and high T range are significantly reduced when the fitting method is used to analyze the observations.

are reflected in our error plots in Figure 4. For example, for given V and T the relative error in $N_{\rm out}$ increases in the range of high N. The misestimation is more pronounced and over a wider range of densities as V increases.

6.2. Potential Improvements

We can overcome some of the limitations mentioned above by using a different technique to analyze the observations. For instance, we can fit the measured distribution function $f_{\rm out}$ with an analytical model as a function of the plasma density, velocity, and temperature $f_{\rm m}$. Several studies fit successfully solar wind observations with various types of distribution functions, such as isotropic Maxwellians (e.g., Elliott et al., 2016) , bi-Maxwellians (e.g., Demars & Schunk, 1990; Stansby et al., 2018) and kappa distribution functions (e.g., Livadiotis, 2017). A typical χ^2 minimization fitting finds the optimal combination of $N_{\rm out}$, $V_{\rm out}$, and $T_{\rm out}$ that minimizes the difference between the analytical expression and the observations:

$$\chi^2 = \sum_{U,\Theta,\Phi} [f(U,\Theta,\Phi) - f_m(N_{out}, V_{out}, T_{out}, U,\Theta,\Phi)]^2. \quad (14)$$

The fitting method accounts for the actual distribution function shape when $f_{\rm out}$ is resolved in limited U,Θ,Φ pixels. In addition, such a routine occasionally overcomes the limitations related to the drifting of the distribution beyond the instrument's energy and field-of-view range, since the fitted model extrapolates for the nonsampled parts of $f_{\rm out}$. In order to test the potential improvement of our results, we derive the plasma parameters by fitting $f_{\rm out}$ with an isotropic Maxwellian model $f_{\rm m}$ (Equation 1). In Figure 10, we show the parameters derived by fitting, along with the corresponding moments, as a function of the plasma T. For the specific test we consider plasma with $N = 10\,{\rm cm}^{-3}$, and $V = 500\,{\rm km\,s}^{-1}$. Our comparison shows that the fitting method improves the accuracy of the derived parameters and therefore is considered as an optimal on-ground analysis method or as an alternative onboard analysis method if the resources allow it. It is important to note, however, that the success of the fitting method requires the right choice of the distribution function model that is used to interpret the observations. Typically, the value of χ^2 indicates the goodness of the fitted model to the observations.

Moreover, we can potentially increase the resolution of the observations by modifying the operation of the instrument. For instance, we can use beam tracking techniques (De Keyser et al., 2018) to obtain the velocity distribution functions of fast and cold solar wind plasma. Such a technique could enable fine energy and/or angular scans of the velocity distribution functions near their peak value, increasing the number of pixels with registered particles.

6.3. Additional Challenges and Limitations

In our study we investigate the basic challenges in monitoring space weather phenomena. The simplified solar wind simulations we use demonstrate and quantify the main sources of errors and indicate the required improvements. However, it could be considerably more challenging to accurately monitor the realistic solar wind. First, the velocities of solar wind particles often follow distribution functions that may be way different from the isotropic Maxwellian functions we consider here. For instance, the VDFs of solar wind protons often exhibit temperature anisotropies, organized by the interplanetary magnetic field (e.g., Marsch, 2006; Verscharen et al., 2019). Although ESAs allow the sampling of the full temperature tensor, the accurate characterization of the temperature anisotropy requires the simultaneous measurement of the magnetic field vector. Some other times, the proton VDFs have elongated high-energy tails which are better described by kappa distribution functions, or they have fast solar wind proton beams propagating along the magnetic field. On one hand, the algorithm that calculates the moments of the VDF still determines the plasma bulk properties regardless of the type of the VDF. On the other hand, an accurate fitting algorithm should explore alternative analytical functions to describe the observations. Such a fitting routine though, if performed on

board, will increase the computational requirements for the mission. On-ground fitting may also be seriously challenging in cases when the required prediction time is very short (e.g., for L_1 monitor applications).

Second, solar wind has a nonnegligible component of alpha particles, which contribute notably in the total ram pressure. Therefore, for a complete solar wind characterization, we may have to resolve the VDFs of alphas as well. Previous studies fit the observed distribution functions. Although space weather monitors may not often require the determination of alpha particle properties, the VDFs of alpha particles usually overlap with the VDFs of protons, making the determination of the proton bulk parameters difficult (e.g., Nicolaou et al., 2014). Nevertheless, future analyses could anticipate such complications by analyzing the observations in a limited energy range (e.g., Nicolaou et al., 2018), which could be determined by proton beam tracking techniques (e.g., De Keyser et al., 2018).

It is also important to note that plasma instruments are not capable of resolving the plasma parameters in time scales shorter than their time resolution. On the other hand, solar wind is extremely dynamic and the VDF of the plasma protons is expected to fluctuate in time scales shorter than 1 s (Cara et al., 2017; De Keyser et al., 2018; Šafránková et al., 2013), which is the sampling time of our design. As a result, each sampled VDF accumulates the turbulent fluctuations within the sampling time, and the plasma parameters are occasionally misestimated (e.g., De Marco et al., 2020; Nicolaou, McComas, Bagenal, Elliott, & Ebert, 2015; Nicolaou et al., 2019; Verscharen & Marsch, 2011). However, for typical turbulent fluctuations, the relative error of the derived parameters is very low (e.g., D'Amicis et al., 2019; Nicolaou et al., 2019).

Finally, our study does not include all the realistic limitations of a typical electronic detector. Although we simulate the response of a detector with a finite dead time, we assume that its output signal is sampled in a much higher rate than the rate of the actual events and the dead time. The realistic response could be much more complicated if the sampling time is comparable to the dead time. Moreover, in a realistic operation we need to account for the time we need to sample consecutive energies and elevation angles, which are controlled by high voltage supplies. Besides the finite time to transit from one voltage to another, we need to account for the time required to get a stable voltage output by the power supply.

7. Conclusions

In this study, we evaluated the performance of a proton plasma ESA design for a space weather mission concept. Our design is based on heritage instruments and complies with the typical mass and power restrictions. We simulated observations, and we analyzed them with standard novel analysis methods to derive the plasma bulk parameters. We quantified the accuracy of the derived parameters by comparing them with those we used to model the observations in the first place. We conclude the following:

1. For a wide range of nominal solar wind conditions, a novel onboard analysis of the measurements can deliver the bulk parameters of the plasma protons with relative uncertainty below 20%.
2. The evaluation of the instrument performance using realistic parameters of ICMEs and fast solar wind streams shows that the derived moments can accurately estimate most of the data points within the intervals of interest. The evaluation, however, indicates a certain parameter range where the relative accuracy of the derived moments drops below 20%.
3. For a certain range of plasma speed and temperature the distribution function is resolved in a limited number of pixels, and the error of the derived moments increases.
4. As the temperature to bulk speed ratio increases, a bigger portion of the distribution function drifts beyond the instrument's energy and/or angular field-of-view range, causing misestimations in the plasma parameters derived from the moments of the distribution function.
5. An alternative onboard or additional on-ground analysis of the observed velocity distribution functions can reduce errors significantly. Here we demonstrate the improvements achieved by using a typical χ^2 minimization algorithm which is more computationally demanding than the simple velocity moment calculator. The selection of the analysis method should be driven from the requirements of the space weather mission concept.
6. Finally, we address numerous limitations that a future space monitor design would possibly have to anticipate. The techniques and the methods we demonstrate here could be modified in order to address more complicated, realistic scenarios.

Appendix A: Measurements of Fast ICMEs

We evaluate our instrument's performance while measuring plasma within fast ICMEs. We consider the plasma bulk parameters for ICMEs observed by ACE and registered in the catalog by Richardson and Cane (2010). We select five ICMEs for which the maximum speed between the time of disturbance and the trailing edge exceeded 1,000 km s^{-1}. For each event, we use ACE observations to model the expected observations by our design, which we then analyze, using a χ^2 minimization fitting to derive the bulk parameters. Figures A1–A5 show the ACE observations for each extreme event, with the color representing the accuracy of the parameters. Here, we consider an isotropic Maxwell distribution to model and fit the observations.

The analysis of fast ICMEs with the χ^2 method reduced significantly the misestimations of the derived plasma parameters. For all the examples we present here, the fitting method determines very accurately the plasma speed. We detect significant misestimations of the plasma density and temperature only at times when the instrument observes very cold ($T < 1$ eV) and relatively fast ($V > 600$ km s^{-1}) plasma. The apparent positive correlation between the speed and temperature of ICMEs eliminates the frequency of these misestimations, especially at the maximum speed of the events. Therefore, the fitting method could be a good candidate to complement or replace the moments analysis method in mission concepts that prioritize the accuracy of the derived parameters within fast ICMEs.

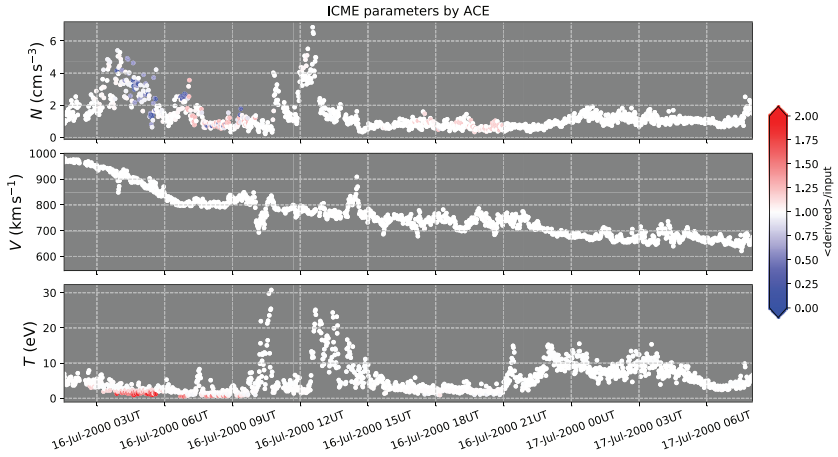

Figure A1. Time series of (top) the plasma density, (middle) bulk speed, and (bottom) scalar temperature within a fast ICME recorded by ACE from 16 July 2000 at 01:00 to 17 July 2000 at 08:00. The color represents the accuracy with which the fitting analysis of the observations by our instrument derives the corresponding parameters.

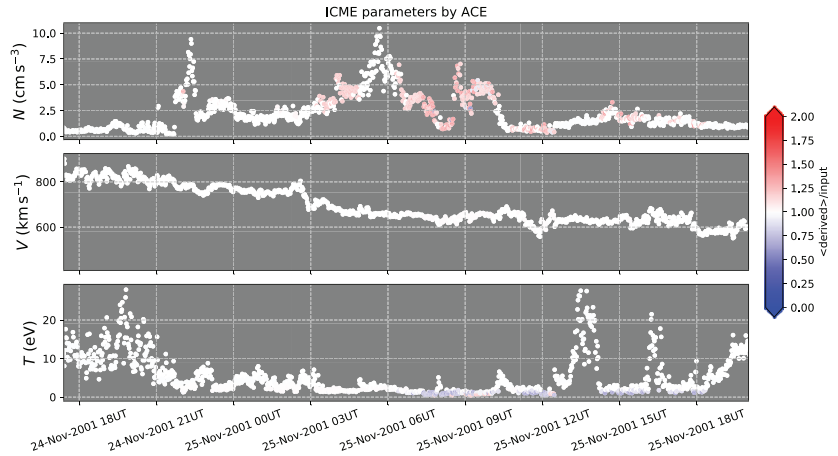

Figure A2. Time series of the plasma bulk parameters for the ICME observed from 24 November 2011 at 17:00 to 25 November 2001 at 20:00. The plot is in the same format as in Figure A1.

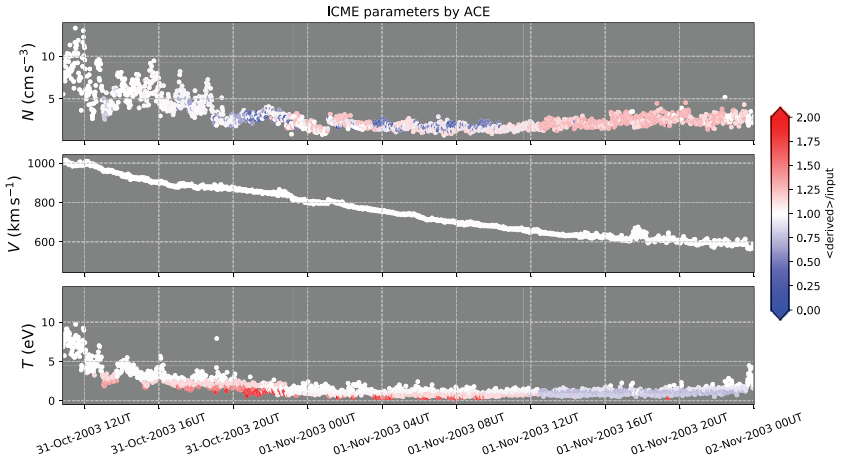

Figure A3. Time series of the plasma bulk parameters for the ICME observed from 31 October 2003 at 11:00 to 2 November 2003 at 00:00. The plot is in the same format as in Figure A1.

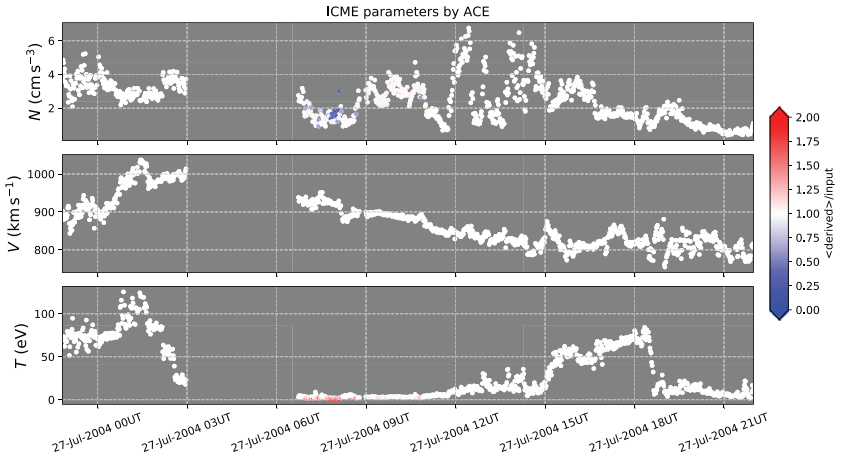

Figure A4. Time series of the plasma bulk parameters for the ICME observed from 26 July 2004 at 22:00 to 27 July 2004 at 22:00. The plot is in the same format as in Figure A1.

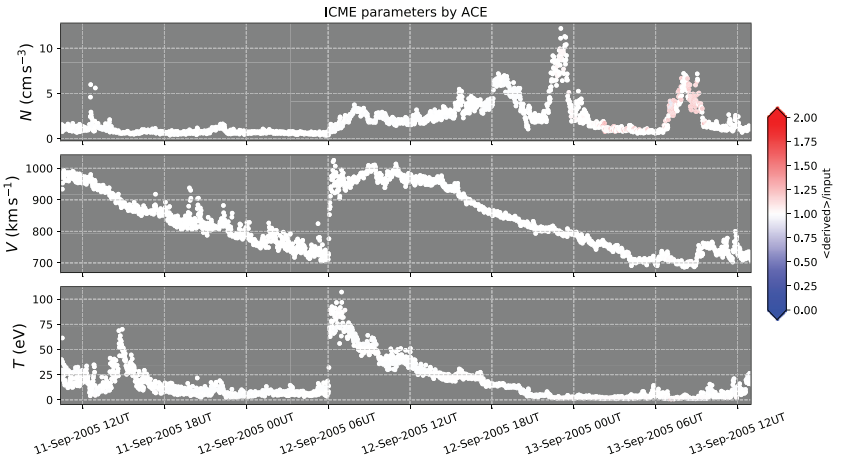

Figure A5. Time series of the plasma bulk parameters for two ICMEs observed from 11 September 2005 at 11:00 to 13 September 2005 at 13:00. The plot is in the same format as in Figure A1.

Appendix B: Measurements of Fast Streams

We evaluate our instrument's performance while measuring fast solar wind streams. We focus on time intervals including measurement of fast streams with maximum speed exceeding 800 kms^{-1} and a background slow solar wind with speed ~400 kms^{-1}. We select four such events (Figures B1–B4), measured by ACE spacecraft and registered by Xystouris et al. (2014).

For all fast solar wind streams we examine here, there is no apparent misestimation of the plasma parameters. Therefore the fitting method can be considered as a method to accurately characterize the plasma parameters when required. For instance, a space weather mission at L_5 possibly should prioritize the accuracy of the plasma density and temperature in such events, where the novel moments calculator will fail to meet the accuracy requirements (see Figure 8).

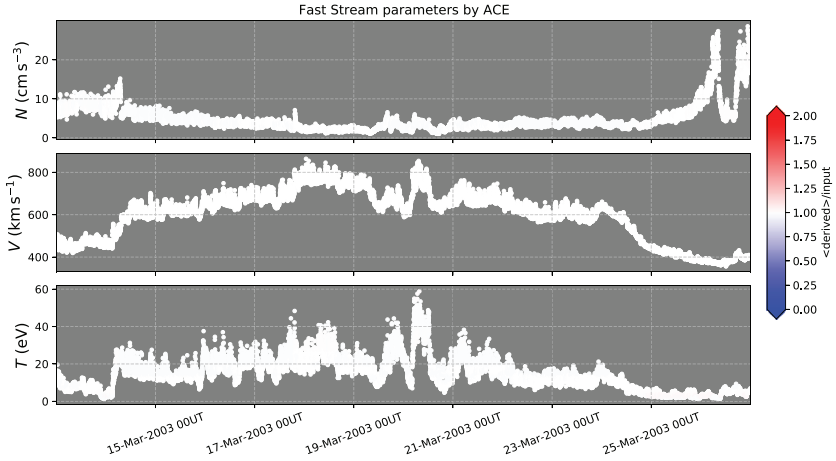

Figure B1. ACE observations of (top) the plasma density, (middle) bulk speed, and (bottom) scalar temperature within the time interval between 13 and 27 March 2003, which includes a fast solar wind stream. The color represents the accuracy with which the fitting analysis of the observations by our instrument derives the corresponding parameters.

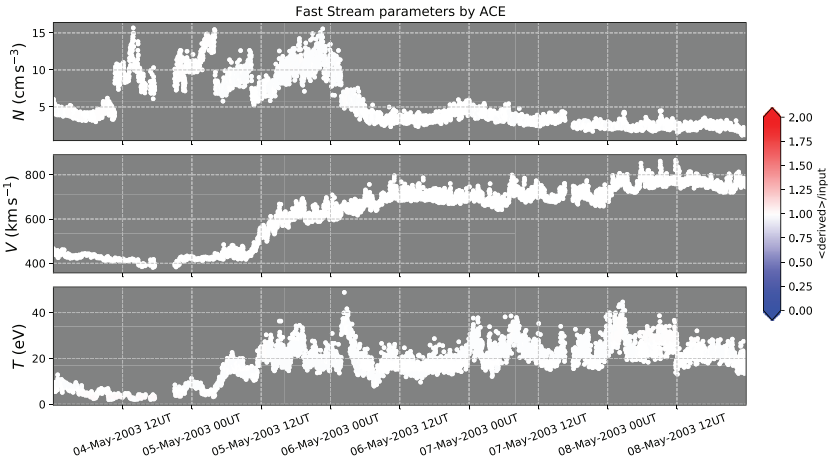

Figure B2. ACE observations of (top) the plasma density, (middle) bulk speed, and (bottom) scalar temperature within the time interval between 4 and 9 May 2003, which includes a fast solar wind stream. The plot is in the same format as in Figure B1.

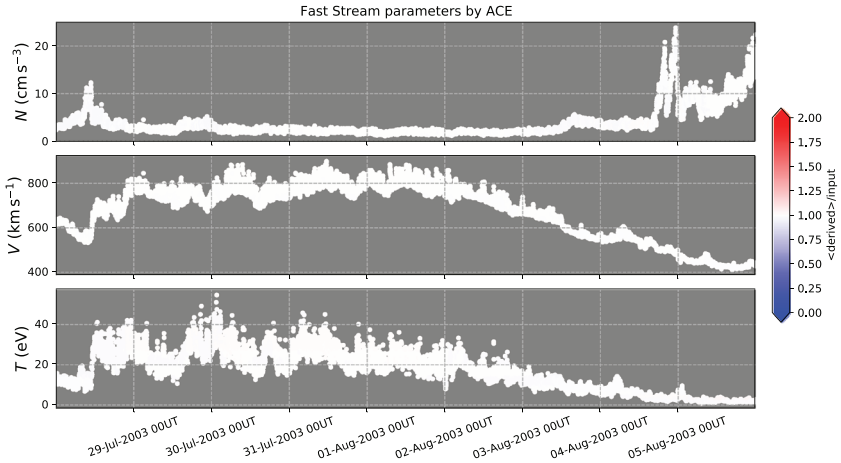

Figure B3. ACE observations of (top) the plasma density, (middle) bulk speed, and (bottom) scalar temperature within the time interval between 28 July 2003 and 6 August 2003, which includes a fast soar wind stream. The plot is in the same format as in Figure B1.

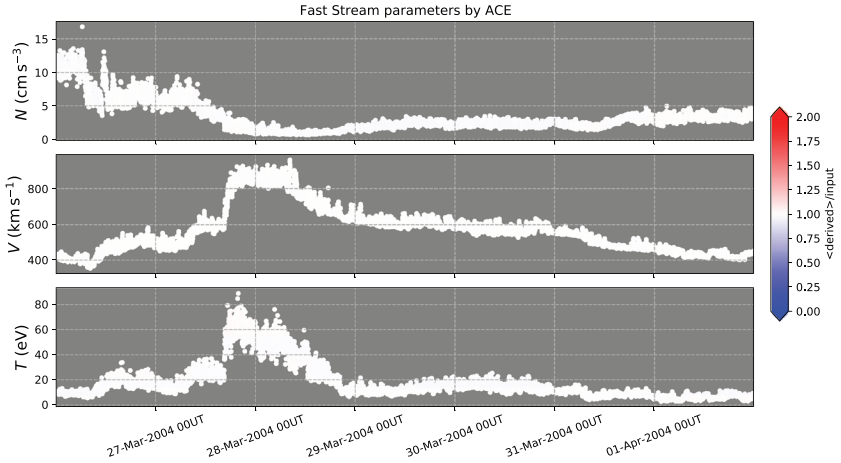

Figure B4. ACE observations of (top) the plasma density, (middle) bulk speed, and (bottom) scalar temperature within the time interval between 26 March 2004 and 2 April 2004, which includes a fast soar wind stream. The plot is in the same format as in Figure B1.

Data Availability Statement

The used data set is publicly available (at https://cdaweb.gsfc.nasa.gov).

Acknowledgments
In this study we use proton plasma data from Advance Composition Explorer (ACE). G. N. is supported by the Consolidated Grant to UCL/MSSL, ST/S000240/1.

References

Akasofu, S.-I. (1964). The development of the auroral substorm. *Planetary and Space Science*, *12*(4), 273–282. https://doi.org/10.1016/0032-0633(64)90151-5

Baker, D. N., Li, X., Pulkkinen, A., Ngwira, C. M., Mays, M. L., Galvin, A. B., & Simunac, K. D. C. (2013). A major solar eruptive event in July 2012: Defining extreme space weather scenarios. *Space Weather*, *11*, 585–591. https://doi.org/10.1002/swe.20097

Barabash, S., Lundin, R., Andersson, H., Brinkfeldt, K., Grigoriev, A., Gunell, H., et al. (2006). The Analyzer of Space Plasmas and Energetic Atoms (ASPERA-3) for the Mars Express mission. *Space Science Reviews*, *126*, 113–164.

Cara, A., Lavraud, B., Fedorov, A., De Keyser, J., DeMarco, R., Marcucci, M. F., et al. (2017). Electrostatic analyzer design for solar wind proton measurements with high temporal, energy, and angular resolutions. *Journal of Geophysical Research: Space Physics*, *122*, 1439–1450. https://doi.org/10.1002/2016JA023269

D'Amicis, R., De Marco, R., Bruno, R., & Perrone, D. (2019). Investigating the nature of the link between magnetic field orientation and proton temperature in the solar wind. *Astronomy and Astrophysics*, *632*, 8. https://doi.org/10.1051/0004-6361/201936728

De Keyser, J., Lavraud, B., Přech, L., Neefs, E., Berkenbosch, S., Beeckman, B., et al. (2018). Beam tracking strategies for fast acquisition of solar wind velocity distribution functions with high energy and angular resolutions. *Annales Geophysicae*, *36*(5), 1285–1302. https://doi.org/10.5194/angeo-36-1285-2018

De Marco, R., Bruno, R., D'Amicis, R., Telloni, D., & Perrone, D. (2020). Possible instrumental effects on moments computation of the solar wind proton velocity distribution function: Helios observations. *Astronomy and Astrophysics*, *639*, 7. https://doi.org/10.1051/0004-6361/201937200

Demars, H. G., & Schunk, R. W. (1990). Solar wind proton velocity distributions: Comparison of the bi-Maxwellian based 16-moment expansion with observations. *Planetary and Space Science*, *38*, 1091–1103. https://doi.org/10.1016/0032-0633(90)90018-L

Elliott, H. A., McComas, D. J., Valek, P., Nicolaou, G., Weidner, S., & Livadiotis, G. (2016). The New Horizons Solar Wind Around Pluto SWAP observations of the solar wind from 11–33 au. *The Astrophysical Journal Supplement Series*, *223*(2), 19. https://doi.org/10.3847/0067-0049/223/2/19

Hapgood, M. (2012). Prepare for the coming space weather storm. *Nature*, *484*, 311–313.

Johnstone, A. D., Alsop, C., Burge, S., Carter, P. J., Coates, A. J., Coker, A. J., et al. (1997). PEACE: A Plasma Electron and Current Experiment. *Space Science Reviews*, *79*, 351–398.

Kessel, R. L., Johnstone, A. D., Coates, A. J., & Gowen, R. A. (1989). Space plasma measurements with ion instruments. *Review of Scientific Instruments*, *60*(12), 3750–3761. https://doi.org/10.1063/1.1141075

Kim, T. K., Ebert, R. W., Valek, P. W., Allegrini, F., McComas, D. J., Bagenal, F., et al. (2020). Method to derive ion properties from Juno JADE including abundance estimates for O^+ and S^{2+}. *Journal of Geophysical Research: Space Physics*, *125*, e2018JA026169. https://doi.org/10.1029/2018JA026169

Knoll, G. F. (2000). *Radiation detection and measurement; 3rd ed*. New York, NY: Wiley.

Liu, Y. D., Luhmann, J. G., Kajdič, P., Kilpua, E. K. J., Lugaz, N., Nitta, N. V., et al. (2014). Observations of an extreme storm in interplanetary space caused by successive coronal mass ejections. *Nature Communications*, *5*, 3481.

Livadiotis, G. (2017). *Kappa distributions: Theory and applications in plasmas*. Amsterdam: Elsevier.

Marsch, E. (2006). Kinetic physics of the solar corona and solar wind. *Living Reviews in Solar Physics*, *3*, 1. https://doi.org/10.12942/lrsp-2006-1

Martz, C., Sauvand, J., & Reme, H. (1993). Accuracy on ion distribution measurements and related parameters using the Cluster CIS experiment. In *paper ESA WPP 07 presented at International Conference on Spatio-Temporal Analysis for Resolving Plasma Turbulence (START)*, pp. 229–236.

McComas, D. J., Alexander, N., Allegrini, F., Bagenal, F., Beebe, C., Clark, G., et al. (2017). The Jovian Auroral Distributions Experiment (JADE) on the Juno mission to Jupiter. *Space Science Reviews*, *213*, 547–643.

McComas, D. J., Bame, S. J., Barker, P., Feldman, W. C., Phillips, J. L., Riley, P., & Griffee, J. W. (1998). Solar Wind Electron Proton Alpha Monitor (SWEPAM) for the Advanced Composition Explorer. *Space Science Reviews*, *86*(1), 563–612. https://doi.org/10.1023/A:1005040232597

McGregor, S. L., Hughes, W. J., Arge, C. N., Odstrcil, D., & Schwadron, N. A. (2011). The radial evolution of solar wind speeds. *Journal of Geophysical Research*, *116*, A03106. https://doi.org/10.1029/2010JA016006

Nicolaou, G., & Livadiotis, G. (2020). Statistical uncertainties of space plasma properties described by kappa distributions. *Entropy*, *22*, 541.

Nicolaou, G., Livadiotis, G., Owen, C. J., Verscharen, D., & Wicks, R. T. (2018). Determining the kappa distributions of space plasmas from observations in a limited energy range. *The Astrophysical Journal*, *864*(1), 3. https://doi.org/10.3847/1538-4357/aad45d

Nicolaou, G., Livadiotis, G., & Wicks, R. T. (2020). On the determination of kappa distribution functions from space plasma observations. *Entropy*, *22*, 212. https://doi.org/10.3390/e22020212

Nicolaou, G., McComas, D. J., Bagenal, F., & Elliott, H. A. (2014). Properties of plasma ions in the distant Jovian magnetosheath using Solar Wind Around Pluto data on New Horizons. *Journal of Geophysical Research: Space Physics*, *119*, 3463–3479. https://doi.org/10.1002/2013JA019665

Nicolaou, G., McComas, D. J., Bagenal, F., Elliott, H. A., & Ebert, R. W. (2015). Jupiter's deep magnetotail boundary layer. *Planetary and Space Science*, *111*, 116–125. https://doi.org/10.1016/j.pss.2015.03.020

Nicolaou, G., McComas, D. J., Bagenal, F., Elliott, H. A., & Wilson, R. J. (2015). Plasma properties in the deep Jovian magnetotail. *Planetary and Space Science*, *119*, 222–232. https://doi.org/10.1016/j.pss.2015.10.001

Nicolaou, G., Verscharen, D., Wicks, R. T., & Owen, C. J. (2019). The impact of turbulent solar wind fluctuations on Solar Orbiter plasma proton measurements. *The Astrophysical Journal*, *886*(2), 101. https://doi.org/10.3847/1538-4357/ab48e3

Nicolaou, G., Wicks, R. T., Livadiotis, G., Verscharen, D., Owen, C. J., & Kataria, D. (2020). Determining the bulk parameters of plasma electrons from pitch-angle distribution measurements. *Entropy*, *22*(1), 103. https://doi.org/10.3390/e22010103

Nilsson, H., Lundin, R., Lundin, K., Barabash, S., Borg, H., Norberg, O., et al. (2007). RPC-ICA: The Ion Composition Analyzer of the Rosetta Plasma Consortium. *Space Science Reviews*, *128*, 671–695.

Oughton, E., Copic, J., Skelton, A., Kesaite, V., Yeo, Z. Y., Ruffle, S. J., et al. (2016). Helios solar storm scenario. Cambridge Risk Framework Series; Center for Risk Studies.

Owen, C. J., Bruno, R., Livi, S., Louarn, P., Janabi, K. A., Allegrini, F., et al. (2020). The Solar Orbiter Solar Wind Analyser (SWA) suite. *Astronomy and Astrophysics*, *642*, 46. https://doi.org/10.1051/0004-6361/201937259

Richardson, I. G., & Cane, H. V. (2010). Near-Earth interplanetary coronal mass ejections during Solar Cycle 23 (1996–2009): Catalog and summary of properties. *Solar Physics*, *264*(1), 189–237. https://doi.org/10.1007/s11207-010-9568-6

Russell, C. T., Mewaldt, R. A., Luhmann, J. G., Mason, G. M., von Rosenvinge, T. T., Cohen, C. M. S., et al. (2013). The very unusual interplanetary coronal mass ejection of 2012 July 23: A blast wave mediated by solar energetic particles. *The Astrophysical Journal*, *770*(1), 38. https://doi.org/10.1088/0004-637x/770/1/38

Schrijver, C. J., Kauristie, K., Aylward, A. D., Denardini, C. M., Gibson, S. E., Glover, A., et al. (2015). Understanding space weather to shield society: A global road map for 2015–2025 commissioned by COSPAR and ILWS. *Advances in Space Research*, *55*(12), 2745–2807. https://doi.org/10.1016/j.asr.2015.03.023

Schwenn, R. (2006). Space weather: The solar perspective. *Living Reviews in Solar Physics*, *3*(1), 2. https://doi.org/10.12942/lrsp-2006-2

Skoug, R. M., Gosling, J. T., Steinberg, J. T., McComas, D. J., Smith, C. W., Ness, N. F., et al. (2004). Extremely high speed solar wind: 29–30 October 2003. *Journal of Geophysical Research*, *109*, A09102. https://doi.org/10.1029/2004JA010494

Stansby, D., Salem, C., Matteini, L., & Horbury, T. (2018). A new inner heliosphere proton parameter dataset from the Helios mission. *Solar Physics*, *293*, 155. https://doi.org/10.1007/s11207-018-1377-3

Stone, E. C., Frandsen, A. M., Mewaldt, R. A., Christian, E. R., Margolies, D., Ormes, J. F., & Snow, F. (1998). The Advanced Composition Explorer. *Space Science Reviews*, *86*(1), 1–22. https://doi.org/10.1023/A:1005082526237

Šafránková, J., Němeček, Z., Přech, L., Zastenker, G., Čermák, I., Chesalin, L., et al. (2013). Fast Solar Wind Monitor (BMSW): Description and first results. *Space Science Reviews*, *175*, 165–182. https://doi.org/10.1007/s11214-013-9979-4

Verscharen, D., Klein, K. G., & Maruca, B. A. (2019). The multi-scale nature of the solar wind. *Living Reviews in Solar Physics*, *16*, 5. https://doi.org/10.1007/s41116-019-0021-0

Verscharen, D., & Marsch, E. (2011). Apparent temperature anisotropies due to wave activity in the solar wind. *Annales Geophysicae*, *29*(5), 909–917. https://doi.org/10.5194/angeo-29-909-2011

Watari, S., Watanabe, T., & Marubashi, K. (2001). Statistical analysis of long-duration low-density solar wind events. *Annales Geophysicae*, *19*(1), 17–23. https://doi.org/10.5194/angeo-19-17-2001

Wilson, R. J., Bagenal, F., & Persoon, A. M. (2017). Survey of thermal plasma ions in Saturn's magnetosphere utilizing a forward model. *Journal of Geophysical Research*, *122*, 7256–7278. https://doi.org/10.1002/2017JA024117

Wilson, R. J., Tokar, R. L., Henderson, M. G., Hill, T. W., Thomsen, M. F., & Pontius Jr., D. H. (2008). Cassini plasma spectrometer thermal ion measurements in Saturn's inner magnetosphere. *Journal of Geophysical Research*, *113*, A12218. https://doi.org/10.1029/2008JA013486

Xystouris, G., Sigala, E., & Mavromichalaki, H. (2014). A complete catalogue of high-speed solar wind streams during Solar Cycle 23. *Solar Physics*, *289*, 995–1012.